Frontiers in Physics

TYPE Original Research
PUBLISHED 25 February 2026
DOI 10.3389/fphy.2026.1768836

OPEN ACCESS

EDITED BY
Imran Khan,
COMSATS Institute of Information Technology, Pakistan

REVIEWED BY
Peican Zhu,
Northwestern Polytechnical University, China
Kemal Gokhan Nalbant,
Beykent University, Türkiye

*CORRESPONDENCE
Hung Tran-Huy,
✉ hung.tran.huy@phenikaa-uni.edu.vn
Darius Andriukaitis,
✉ darius.andrikaitis@ktu.lt

RECEIVED 16 December 2025
REVISED 09 January 2026
ACCEPTED 16 January 2026
PUBLISHED 25 February 2026

CITATION
Sani MAA, Sani NS, Prauzek M, Konecny J, Tran-Huy H, Hoang-Thu T, Qaddara I, Mohamed HG and Andriukaitis D (2026) Low-profile miniaturized dielectric resonator array antenna design for frequency division duplex based on sequential rotation method. *Front. Phys.* 14:1768836. doi: 10.3389/fphy.2026.1768836

Low-profile miniaturized dielectric resonator array antenna design for frequency division duplex based on sequential rotation method

Mohd Aliff Afira Sani[1], Nor Samsiah Sani[2], Michal Prauzek[3], Jaromir Konecny[3], Hung Tran-Huy[4]*, Trang Hoang-Thu[4], Iyas Qaddara[5], Heba G. Mohamed[6] and Darius Andriukaitis[7]*

[1]Quality Engineering Research Cluster (QEREC), Universiti Kuala Lumpur, Malaysian Institute of Industrial Technology, Kuala Lumpur, Malaysia, [2]Center for Artificial Intelligence Technology, Faculty of Information Science and Technology, Universiti Kebangsaan, Kajang, Malaysia, [3]Department of Cybernetics and Biomedical Engineering, VSB-Technical University of Ostrava, Ostrava, Czechia, [4]Faculty of Electrical and Electronic Engineering, PHENIKAA School of Engineering, PHENIKAA University, Hanoi, Vietnam, [5]Department of Computer Science, Faculty of Information Technology, Al-Ahliya Amman University, Amman, Jordan, [6]Department of Electrical Engineering, College of Engineering, Princess Nourah bint Abdulrahman University, Riyadh, Saudi Arabia, [7]Department of Electronics Engineering, Kaunas University of Technology, Kaunas, Lithuania

Introduction: The antenna must adhere to more stringent requirements, including multi-band operation, high performance, and compact design, since it is the primary component of satellite communication systems. A shared-aperture antenna based on structural reuse is a viable method for attaining multi-band functionality of satellite communication systems and improving platform space usage. The development of multi-function antennas, antenna size reduction for shrinking, and cost reduction are all greatly impacted by shared-aperture technology. Because of the significance of L-band applications, the development of circularly polarized (CP) antennas has grown in importance. Because of their compensations, which include lower multipath losses and polarization mismatch, CP antennas are essential for many wireless applications, such as GNSS, satellite communication, and indoor wireless systems.

Methods: This paper proposes a novel dielectric resonator array antenna. The shared-aperture feature is established by merging the dielectric high-frequency resonators in the annular dielectric low-frequency resonators. By controlling the phase difference between the degenerate modes, the low and high frequency orthogonal circularly polarized waves are created. The impedance matching is improved by optimizing the thickness of the circular cylindrical dielectric resonator. The sequential rotation method is used to design the array antenna.

Results and Discussion: Simulation results show that the proposed dielectric resonator array antenna has superior performance and improved polarization characteristics as compared with existing methods.

KEYWORDS

airborne antenna, array antenna, beamforming, circular polarization, dielectric resonator antenna, dual-band waveguide, metamaterial

1 Introduction

With the integration and development of mobile and satellite communications, the sixth generation (6G) of mobile communication systems will integrate ground networks and non-ground networks to build an integrated air-ground-space system [1]. Antennas are essential to the operation of communication systems since they are one of the main parts that link wireless channels and hardware communication devices. Excellent dual-frequency dual-circular polarization functions—that is, the ability to send and receive orthogonal circularly polarized electromagnetic waves in the uplink and downlink frequency bands—are necessary for ground terminal antennas to meet the demands of satellite Internet for high-speed duplex communication. In traditional satellite antenna technology, the transmitting array and the receiving array are independent of each other, resulting in the problem of large physical size of the antenna feed system. The design of a miniaturized co-aperture dual-frequency dual-circular polarization antenna is one of the important basic technologies for the rapid commercialization of non-ground networks in the future.

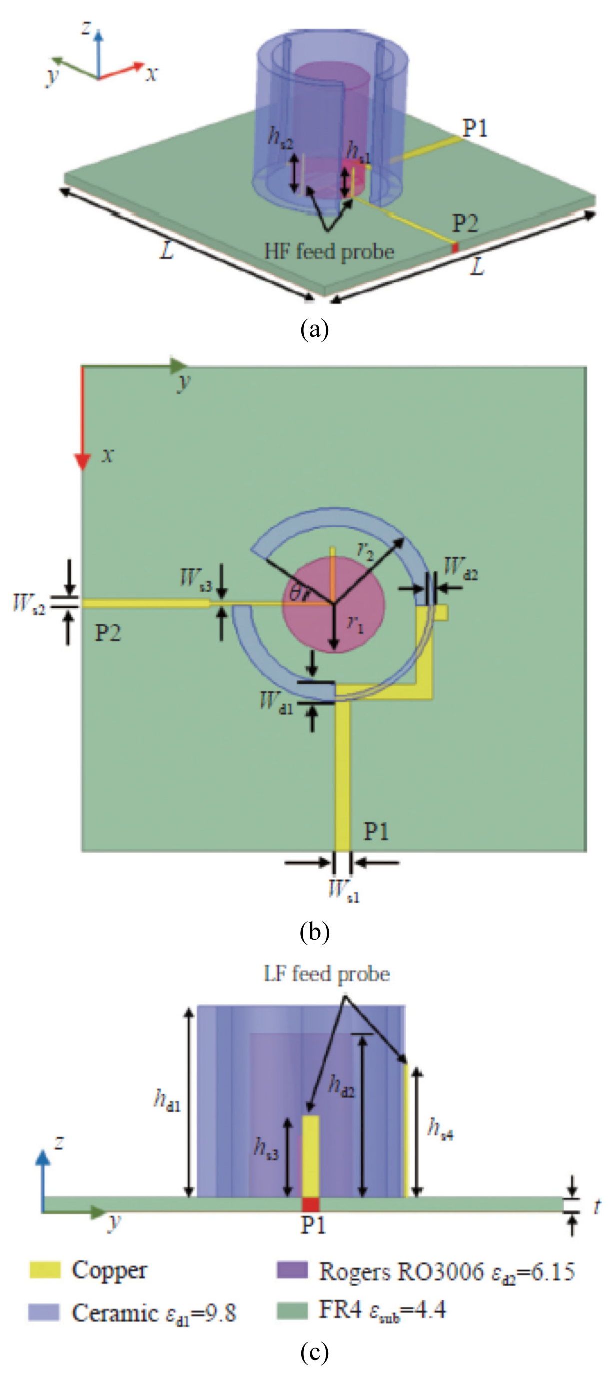

FIGURE 1
Unit structure design. **(a)** 3D view; **(b)** top view; **(c)** side view.

TABLE 1 Design parameters of unit structure.

Parameter	Value (mm)
L	13.750
h_{s1}	1.2
h_{s2}	1.72
w_{s1}	0.45
w_{s2}	0.24
w_{s3}	0.12
r_1	1.375
r_2	2.75
w_{d1}	0.5
w_{d2}	0.15
h_{s3}	2.25
h_{s4}	3.65
h_{d1}	5.25
h_{d2}	4.5
t	0.4

Based on the traditional microstrip patch antenna technology, a large number of circularly polarized antenna design methods have been developed. Dual-frequency dual circular polarization can be achieved by adding perturbations to the patch and using improved coupling slots [2–5]. Similar functions can also be achieved by connecting patches of different frequencies and different circular polarization types [6–8]. Reference [8] designed a dipole antenna using two sets of short-circuited patches of different sizes, which can be used in frequency division duplex communication systems. Although patch antennas have the advantage of low profile, their bandwidth is limited and the horizontal aperture is usually too large.

Compared with metal structure patch antennas and reflector antennas, dielectric resonator antennas (DRA) have the advantages of diverse shapes, flexible design, low loss and high efficiency [9, 10]. Reference [11] proposed a broadband low-profile DRA with small planar size, and further expanded its application in the design of

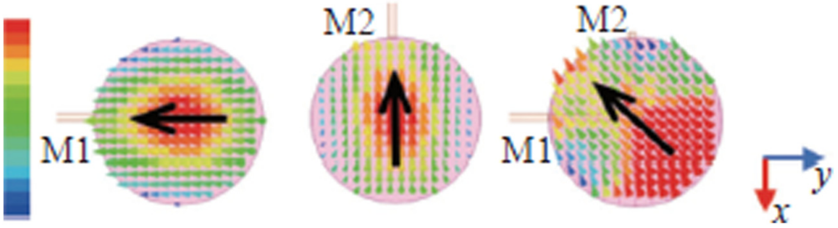

FIGURE 2
Evaluation of electric field distribution under different probe feeding conditions.

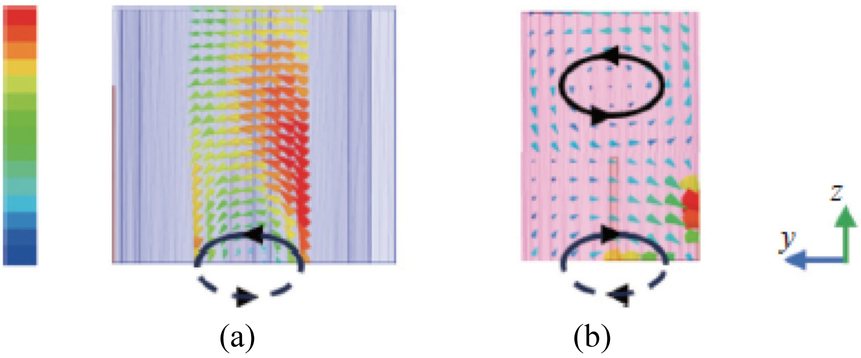

(a)

(b)

FIGURE 3
Evaluation of electric field distribution (*yOz* plane). **(a)** Low-frequency DR at 16.8 GHz; **(b)** High-frequency DR at 27 GHz.

circularly polarized antennas. Reference [12] designed a decorative DRA for video surveillance systems. Simultaneously, dual-frequency dual circularly polarized antennas can be designed using the multi-mode properties of DRA. By loading parasitic units on DRA [13] or by employing a unique dielectric resonator (DR) and a unique feeding structure [14, 15], dual-frequency dual circular polarization can be accomplished in DRA. Reference [16] uses a patch, a substrate integrated cavity and two resonators to form an antenna that can transmit and receive. Reference [17] proposed a shared aperture merging structure technology based on DRA and slot dipole antenna to realize a dual-frequency dual circular polarization antenna.

A co-aperture, dual-frequency, dual-circularly polarized antenna (DRA) appropriate for satellite communication terminals is proposed in this study. The main contributions are as follows.

1. A nested design of annular and cylindrical DRs achieves a co-aperture structure for low- and high-frequency radiators.
2. Metal strip probes of unequal heights are used to excite high-order circular polarization in the high- and low-frequency DRAs.
3. By optimizing the low-frequency radiator structure, high- and low-frequency electromagnetic mutual coupling is reduced, improving the antenna's operating bandwidth and radiation performance.
4. A sequential rotation array method is used to construct a 2 × 2 dual-frequency, dual-circularly polarized antenna array.
5. A prototype was fabricated and tested using ceramic and printed circuit board (PCB) technology. Measurement results demonstrate the antenna's compactness and dual-frequency capabilities, making it suitable for future satellite communication ground terminals.

The remainder of this paper is organized as follows. In Section 2, the unit structure of the antenna is discussed, the optimization process and geometrical design analysis is explained. In Section 3, the antenna unit performance is evaluated through simulations and measurements. In Section 4, antenna array design is presented. In Section 5, the array antenna performance is evaluated using simulations and experimental setup. In Section 6, the conclusions are presented.

2 Antenna design

2.1 Unit structure

Two DRs with differing dielectric constants and a single-layer PCB make up the proposed DRA. Figure 1 depicts the antenna unit structure. The ceramic used to make the hollow low-frequency annular cylindrical DR has a relative dielectric constant of 9.8 [18, 19]. The inner high-frequency cylindrical DR is made of Rogers RO3006 with a relative dielectric constant of 6.15. The two DRs are nested. Two metal strips with a 90° feed phase difference are used on the sidewalls of both the low-frequency and high-frequency DRs for probe feeding. An L-shaped microstrip line that is one-quarter wavelength long connects the two feed probes. The low-frequency

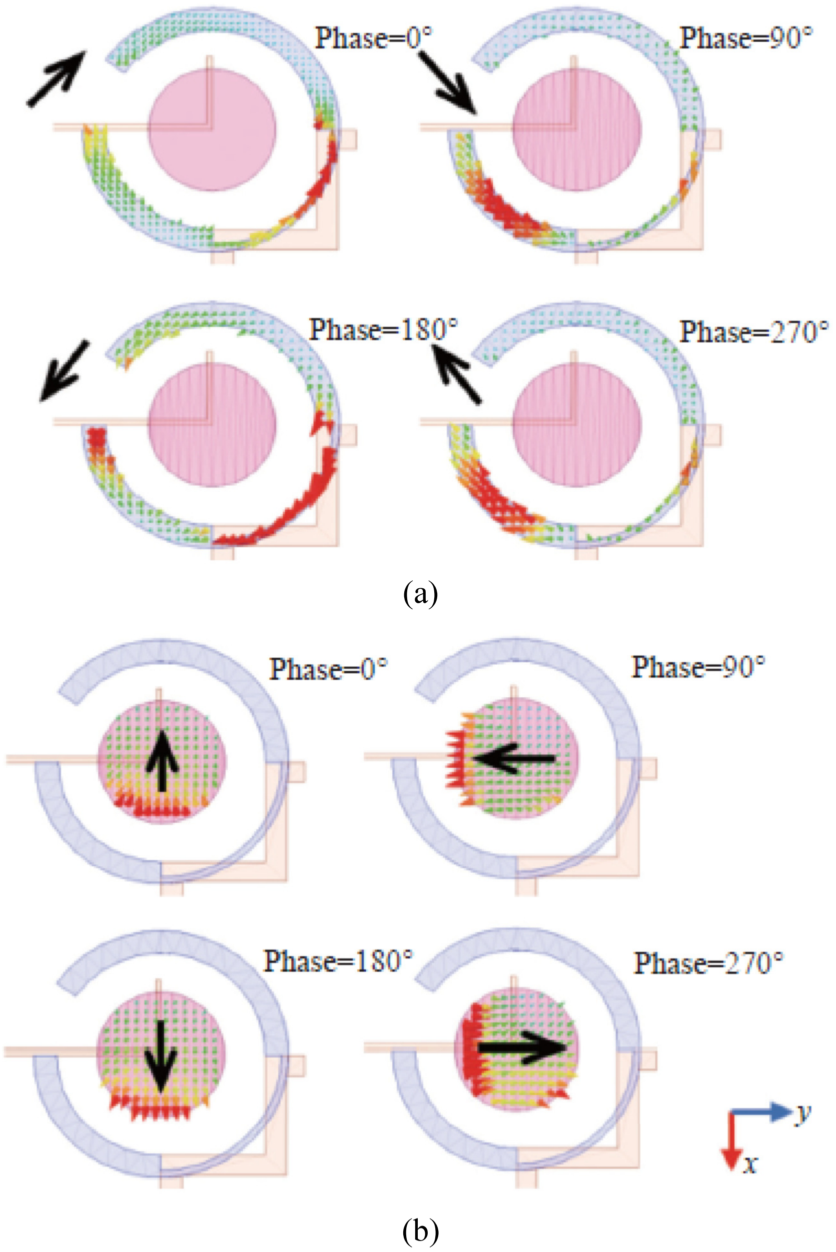

FIGURE 4
Evaluation of electric field distribution (*xOy* plane). **(a)** LF DR at 16.8 GHz; **(b)** HF DR at 27 GHz.

microstrip line is bent in order to avoid overlap with the high-frequency DR. The low-frequency and high-frequency feeding ports are labeled P1 and P2, respectively [20]. The PCB is made of FR4, which has a dielectric constant of 4.4 and a loss tangent of 0.02. The structural parameters of the antenna unit are shown in Table 1, where the cut angle θ = 35°.

2.2 Design principle

Given a satellite communication operating frequency band, the base radius and height of a typical cylindrical DRA can be calculated using Equation 1:

$$f_{\mathrm{res}} = \frac{6.321c}{\pi d\sqrt{\varepsilon_{\mathrm{eff}}+2}}\left[0.27+0.36\left\{\frac{d}{4h_{\mathrm{eff}}}\right\}+0.02\left\{\frac{d}{4h_{\mathrm{eff}}}\right\}\right] \tag{1}$$

Where: c represents the speed of light in free space; d denotes the diameter of the cylinder; $\varepsilon_{\mathrm{eff}}$ is the equivalent dielectric constant of DR; h_{eff} is the equivalent height of the cylinder [21, 22]. The formulas for calculating the dielectric constant and height are expressed in Equation 2:

$$\varepsilon_{\mathrm{eff}} = \frac{h_{\mathrm{eff}}}{h_{\mathrm{CDRA}}/\varepsilon_{\mathrm{CDRA}} + h_{\mathrm{sub}}/\varepsilon_{\mathrm{sub}}} \tag{2}$$

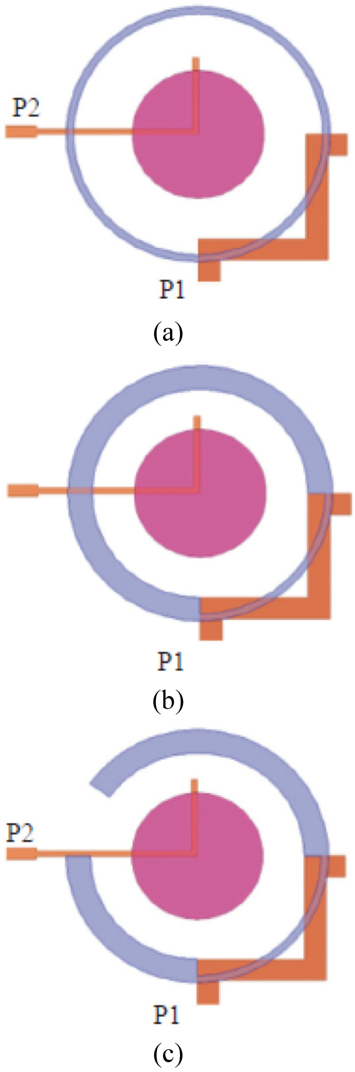

FIGURE 5
Antenna structure optimization process. **(a)** Antenna A; **(b)** Antenna B; **(c)** Antenna C.

Where: h_{CDRA} and h_{sub} are the heights of DR and dielectric substrate respectively; ε_{CDRA} and ε_{sub} are the dielectric constants of DR and dielectric substrate, respectively.

This paper first excites the degenerate modes of a DRA using a dual-point feeding method. Circular polarization is then achieved by feeding the two degenerate modes orthogonally, with identical amplitude and a 90° phase difference, by optimizing the feeding microstrip line [23, 24]. The high-frequency DR is fed in the y and x directions, respectively, by metal strip probes M1 and M2 to produce two orthogonal degenerate modes. Figure 2 depicts the high-frequency DR's electric field distribution pattern at 27 GHz. It can be seen that when only M1 or M2 is loaded on the DR, the DR radiation exhibits linear polarization along the y or x direction. When both M1 and M2 are loaded on the DR, the electric field distribution exhibits a superposition of two linear polarizations in the y and x directions. Thus, circularly polarized radiation can be produced by varying the length of the microstrip line between the two feeding probes to create a 90° phase difference between the two linear polarizations.

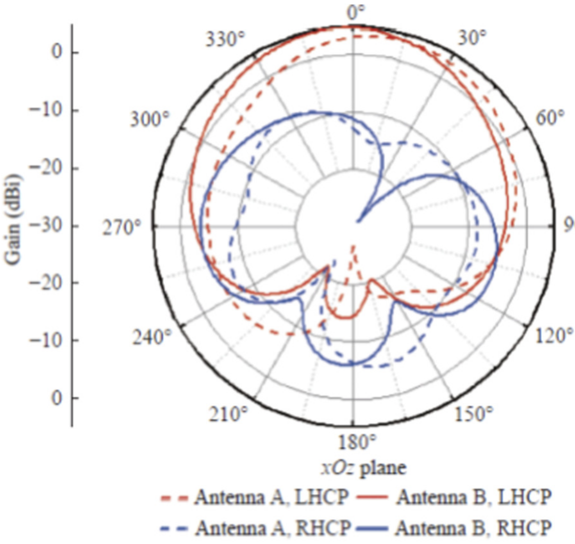

FIGURE 6
Radiation performance of antennas A and B under low frequency.

A nested radiator technique was used to create a co-aperture design for low- and high-frequency antennas in order to satisfy the downsizing criteria of dual-band antennas for satellite communication terminals. A right-hand circularly polarized (RHCP) high-frequency cylinder DRA was nested into a hollow cylindrical structure created by modifying the left-hand circularly polarized (LHCP) low-frequency radiator, which was based on the traditional cylindrical DRA [25]. This resulted in a co-aperture dual-band, dual-circularly polarized design, which decreased the antenna's horizontal dimensions. Figure 3 shows the electric field distribution in the yOz plane of a co-aperture dual-band, dual-circularly polarized antenna operating at 16.8 GHz and 27 GHz, respectively. Based on the mirror image principle and the electric field vector distribution characteristics, the DRA exhibits a HEM$_{10\delta}$ mode at both resonance points [26]. Furthermore, observation of the internal field distribution of the DRA reveals that the antenna's specific operating modes at low and high frequencies are $\delta = 1$ and $\delta = 3$, respectively.

Figure 4 shows the electric field distribution in the xOy plane for a co-aperture dual-band, dual-circularly polarized antenna operating at 16.8 GHz and 27 GHz, respectively. When the antenna operates at low and high frequencies, the electric field in the xOy plane rotates clockwise and counterclockwise as the phase state changes through 0, T/4, T/2, and 3T/4, respectively [27]. This demonstrates that the antenna operates in the LHCP and RHCP states at low and high frequencies, respectively.

2.3 Antenna structure and optimization process

Degraded antenna performance results from electromagnetic mutual interaction between the low-frequency and high-frequency

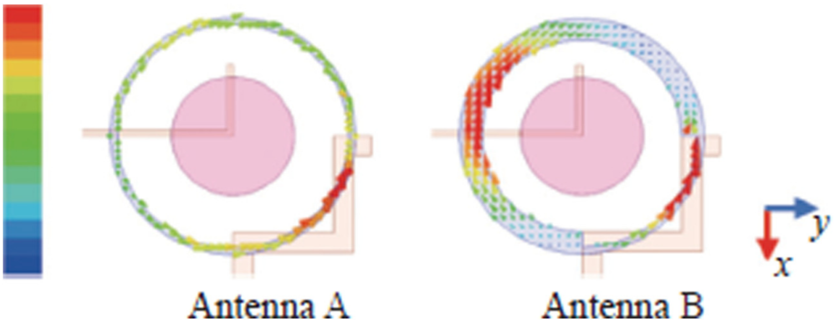

FIGURE 7
Evaluation of electric field distribution at 16.8 GHz in *xOy* plane.

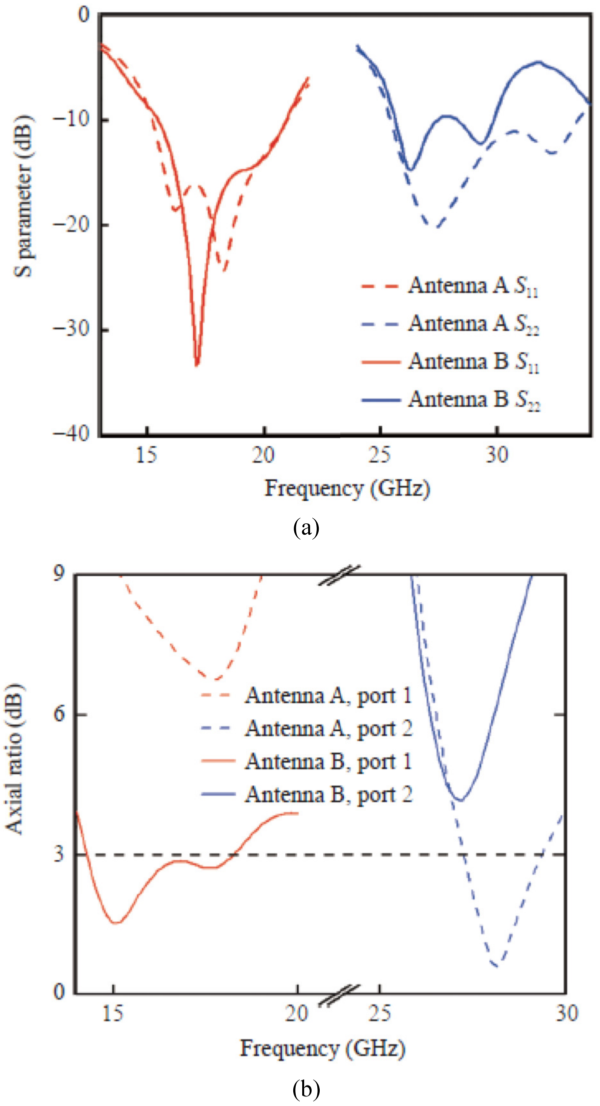

FIGURE 8
Comparison of antennas A and B performance. **(a)** S parameter; **(b)** axial ratio.

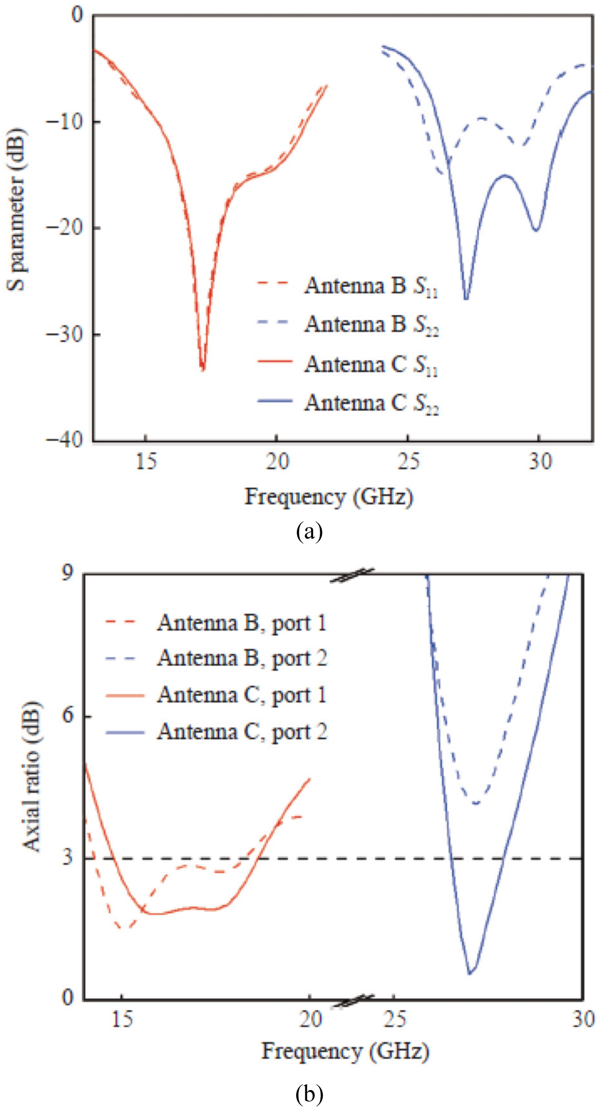

FIGURE 9
Comparison of antennas B and C performance. **(a)** S parameter; **(b)** axial ratio.

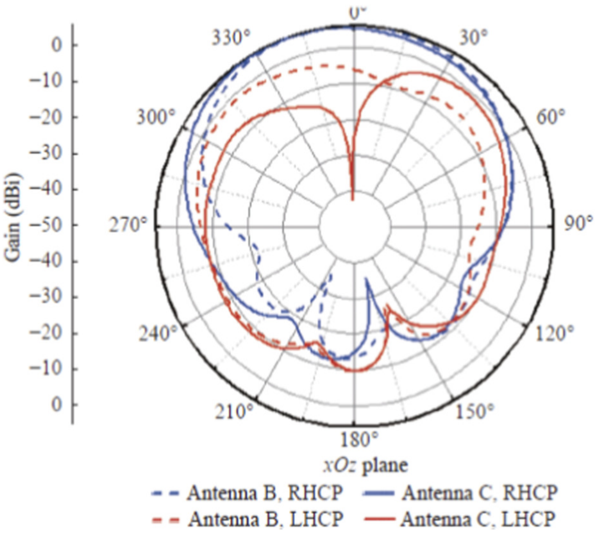

FIGURE 10
Radiation performance comparison of antennas B and C.

radiators in a nested antenna. To optimize the performance [28], the low-frequency radiator's structure was optimized, as shown in Figure 5.

2.3.1 Thickened low-frequency DR section design

Figure 6 shows the simulated low-frequency patterns of Antenna A and Antenna B. Antenna A's asymmetric feed structure affects its radiation performance, resulting in a skewed pattern. By thickening the low-frequency DR section, Antenna B achieves this skewed pattern. Figure 7 evaluates the electric field distribution of the low-frequency DR on the *xOy* plane at 16.8 GHz. It can be concluded that the electric field on the lower right side of Antenna A is significantly stronger than in other areas [29]. In Antenna B, which has a partially thickened low-frequency DR section, the electric field amplitude is symmetrically distributed. The simulation results show that the skewed low-frequency pattern is successfully resolved by the partial thickening method. Figure 8 illustrates that while partially thickening the low-frequency DR section enhances the impedance matching and axial ratio at low-frequency, it marginally deteriorates the impedance matching and axial ratio at high-frequency, necessitating additional optimization.

2.3.2 Low frequency ring DR notch design

The transition from Antenna A to Antenna B solves the problems of narrow low-frequency axial ratio bandwidth and skewed radiation patterns, but it also degrades impedance matching and circular polarization purity at high frequencies. Because the low-frequency DR in Antenna B is placed above the high-frequency feed microstrip line, strong electromagnetic coupling when feeding the high-frequency port causes high-frequency resonance in the microstructure of the low-frequency DR, resulting in degraded impedance matching and axial ratio at high frequencies [30]. Therefore, improving Antenna B to Antenna C can avoid coupling interference from low-frequency radiation to high-frequency radiation. As shown in Figure 9, the notch design in the low-frequency DR improves high-frequency axial ratio and impedance matching. As depicted in Figure 10, Antenna C achieves better polarization purity than Antenna B, with cross-polarization suppression exceeding 40 dB in the main radiation direction [31–33].

3 Antenna unit experimental results and analysis

As shown in Figure 11, a dual-band, dual-circularly polarized DRA prototype was developed and tested to validate the proposed design [34–36]. The measurement findings in Figure 12 show that the antenna unit's low-frequency and high-frequency operational bandwidths are 18.8% (15.4–18.6 GHz) and 5.2% (26.4–27.8 GHz), respectively. The antenna unit's maximum left-hand and right-hand gains are 4.3 dBi and 6.8 dBi, respectively. As seen in Figure 13, the antenna unit radiates RHCP waves with a gain of 6 dBi at 27 GHz and LHCP waves with a gain of 4.1 dBi at 16.8 GHz with good polarization purity [37–39]. The intended design is in line with the measured results.

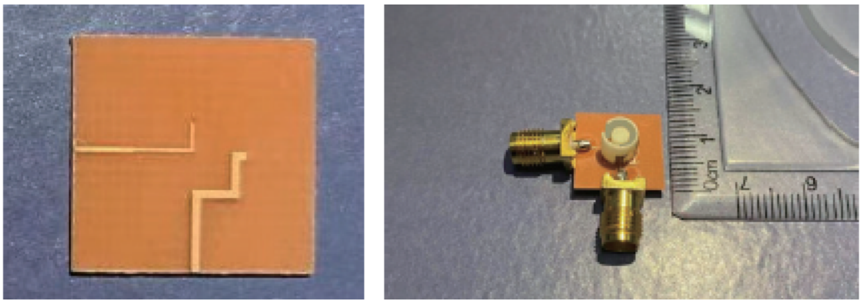
(a) (b)

FIGURE 11
Implemented antenna unit. **(a)** Feeding module; **(b)** antenna unit.

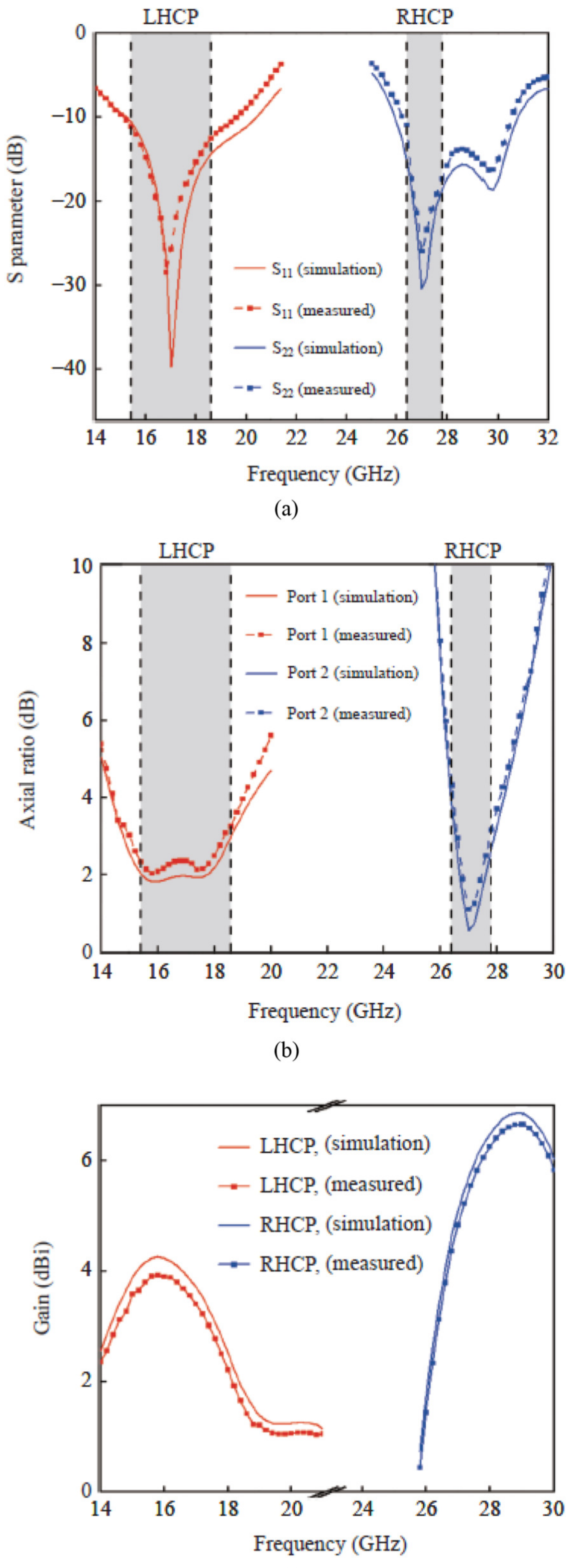

(c)

FIGURE 12
Comparison of simulated and measured performance of the antenna unit. **(a)** S parameter; **(b)** axial ratio; **(c)** gain.

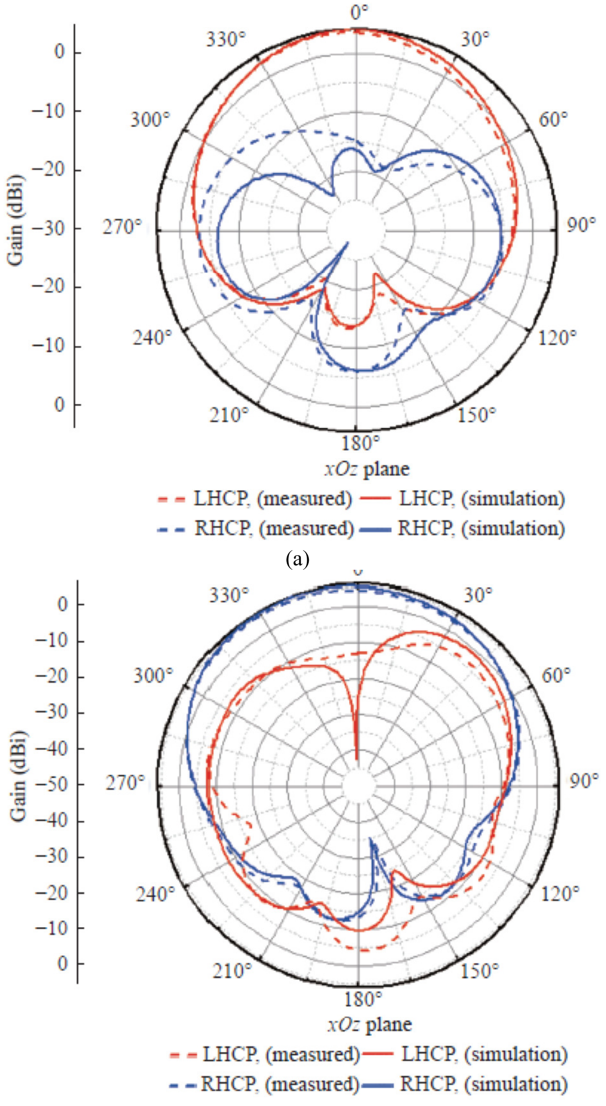

(b)

FIGURE 13
Comparison of radiation performance of the antenna unit under different frequencies. **(a)** 16.8 GHz; **(b)** 27 GHz.

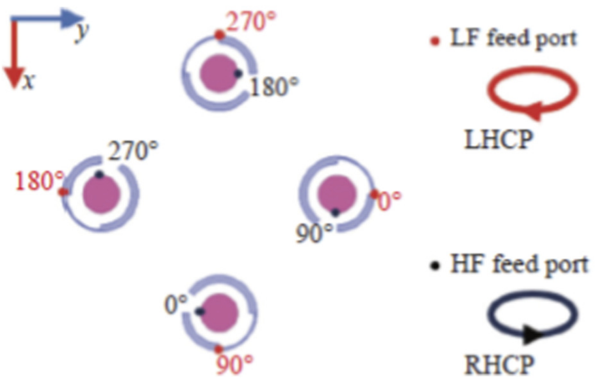

FIGURE 14
Illustration of sequential rotation process.

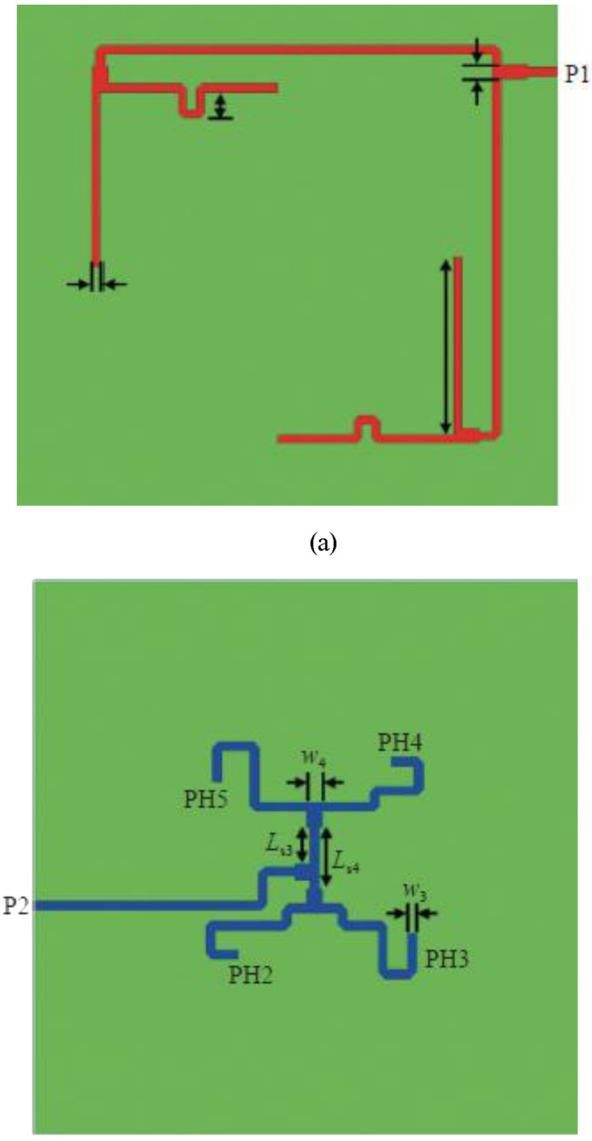

(a)

(b)

FIGURE 15
Power feeding structure. **(a)** Low-frequency; **(b)** High-frequency.

4 Antenna array design

4.1 Sequential rotation technique

The antenna elements are expanded into a 2 × 2 array using sequential rotation technology to further increase the axial ratio bandwidth and antenna gain [40–42]. The successively rotated elements’ circular polarization direction must stay in line with the element; otherwise, the antenna array will experience a radiation null in the direction of maximum radiation. The schematic diagram of the two-port sequential rotation is depicted in Figure 14. The four antenna elements are rotated 90° around the center, with the main radiation direction of the antenna array

TABLE 2 Feeding structure parameters.

Parameter	Value (mm)
w_1	0.75
w_2	1.3
L_{s1}	2.48
L_{s2}	16.2
w_3	0.77
w_4	1.34
L_{s3}	3.41
L_{s4}	5.66

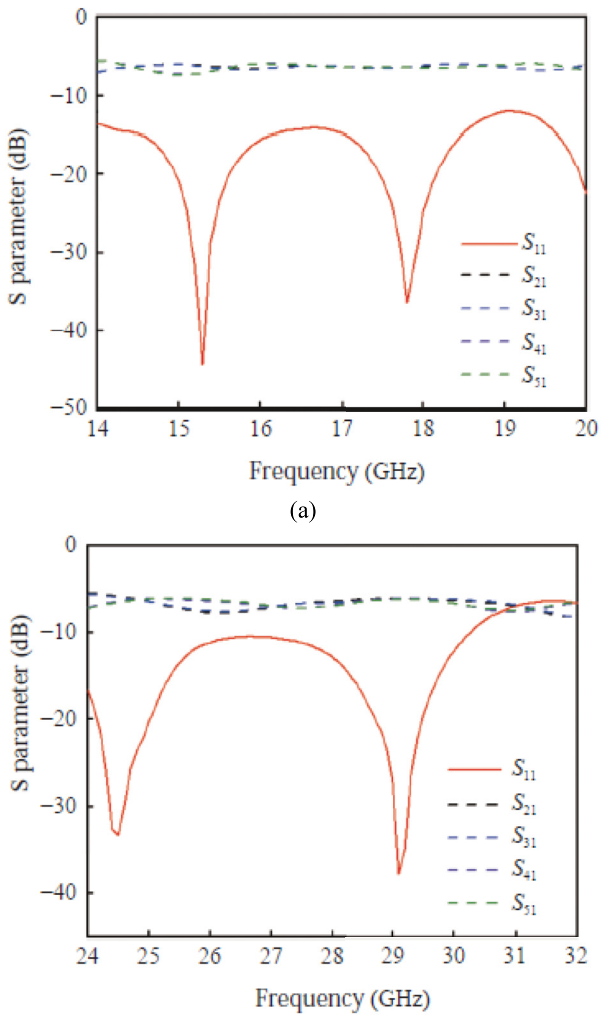

(a)

(b)

FIGURE 16
S-parameter evaluation of the feeding structure. **(a)** Low-frequency; **(b)** High-frequency.

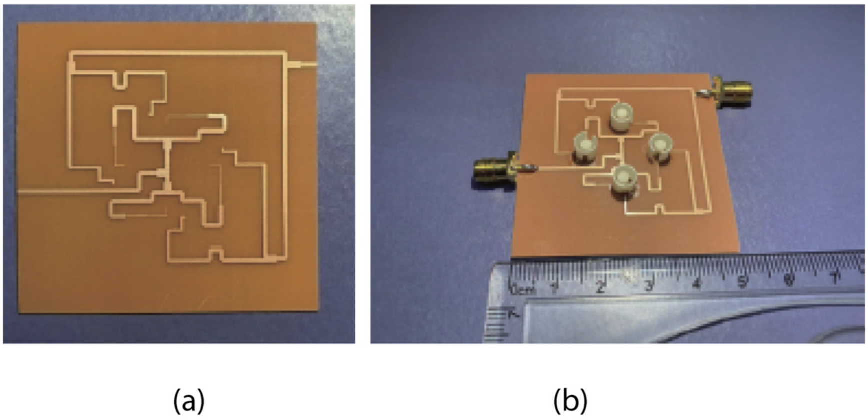

FIGURE 17
Array antenna prototype. **(a)** Feeding structure; **(b)** Array prototype.

being the +z direction [43–45]. The low-frequency feed phases are rotated clockwise to 0°, 90°, 180°, and 270°, respectively, to achieve left-hand circular polarization. The high-frequency feed phases are rotated counterclockwise to 0°, 90°, 180°, and 270°, respectively, to achieve right-hand circular polarization [46–48].

4.2 Feed network design

Due to the limited spatial space of the antenna array, different feed network structures were used for high and low frequencies, as indicated in Figure 15. In the low-frequency feed network, the phases of the power divider's four output ports, PL2 through PL5, increase by 90° in a clockwise orientation [49–51]. The phases of the power divider's four output ports, PH2 through PH5, increase by 90° in an anticlockwise direction in the high-frequency feed network. Table 2 shows the physical dimensions of the power divider. The simulated S-parameter values for the two power dividers are shown in Figure 16. It can be seen that the power dividers operating in different frequency bands have excellent impedance matching and power distribution performance [52–54].

5 Antenna array test results and analysis

To validate the proposed design, a dual-band, dual-circularly polarized DRA array prototype was built and tested, as shown in Figure 17. Figure 18a shows the S-parameter [55–57]. Figure 18b shows that the antenna array's low-frequency and high-frequency operating bandwidths are 25.5% (14.4–18.6 GHz) and 6.5% (26.8–28.6 GHz), respectively. The antenna array's maximum left-hand and right-hand gains are 7.7 dBi and 14 dBi, respectively, according to Figure 18c [58–60]. As seen in Figure 19, the antenna array has good cross-polarization and radiates LHCP waves with a gain of 7 dBi at 17 GHz and RHCP waves with a gain of 13.3 dBi at 28 GHz [61–63]. There is good agreement between the modeling results and the measured data [64–66].

The results of a comparison between the antenna unit and array proposed in this paper and antennas from previous sources are displayed in Table 3 [67–69]. The operating bandwidth in this instance is the point where the axial ratio bandwidth and the impedance bandwidth intersect [70–72]. Table 3 shows that the proposed antenna achieves dual-band, dual-circular polarization performance and has a certain advantage in operating bandwidth [73–75]. When the antenna unit is expanded into an antenna array, the antenna gain has a significant advantage over other antennas, making it suitable for satellite communication terminals [76–78].

6 Conclusion

This paper proposes a common-aperture dual-frequency dual-circular polarization DRA for satellite communication, leveraging the low loss and high efficiency characteristics of DRAs. The Hemian mode is excited and circularly polarized waves are radiated through a microstrip transmission line at the bottom of the cylindrical DR and metal strips of unequal length loaded on its sides. A common-aperture structure is formed by nesting cylindrical DRs within the cylindrical DR, meeting the miniaturization requirements of satellite communication terminals. The antenna's overall performance is enhanced by cutting and partially thickening the low-frequency DR to lessen electromagnetic interaction between high and low frequencies. The antenna is appropriate for upcoming high-speed satellite internet terminals due to its good impedance matching, high gain within its frequency band, and good polarization purity, according to simulation and measured results. Further research considers port merging based on this design, achieving dual-frequency dual-circular polarization through a single-feed method.

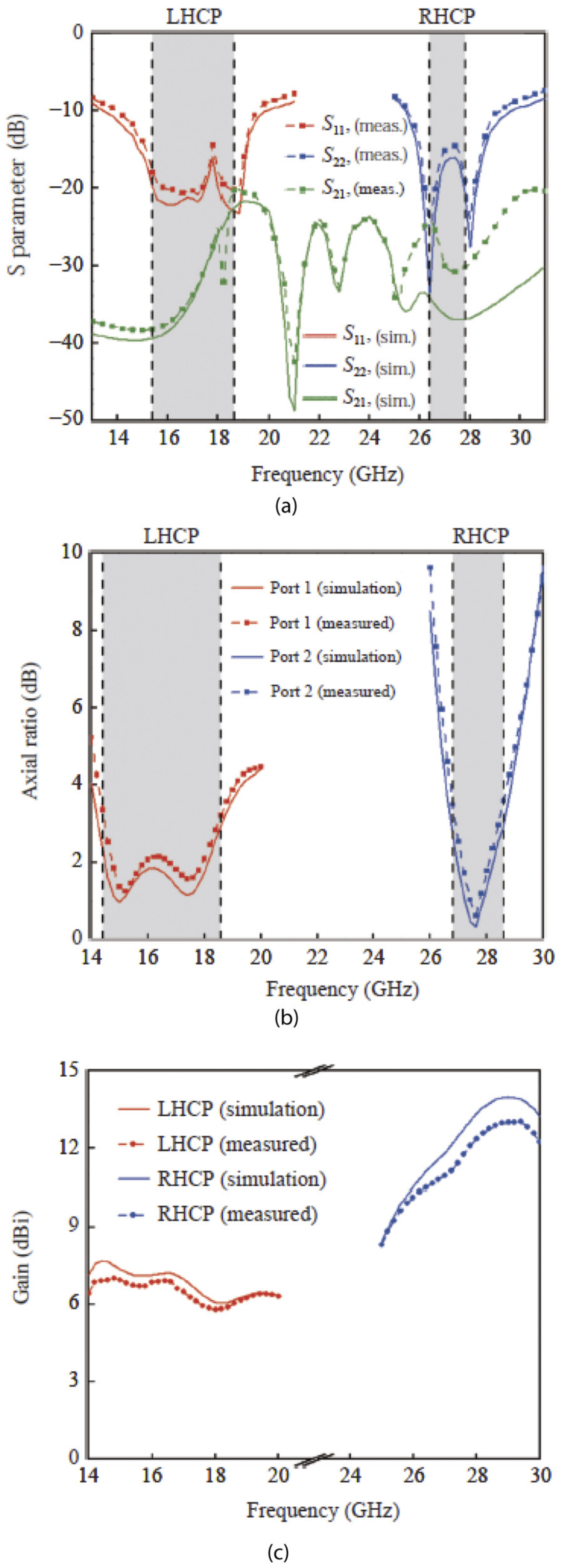

FIGURE 18
Comparison of simulated and measured performance of the antenna array. **(a)** S-parameter; **(b)** axial ratio; **(c)** gain.

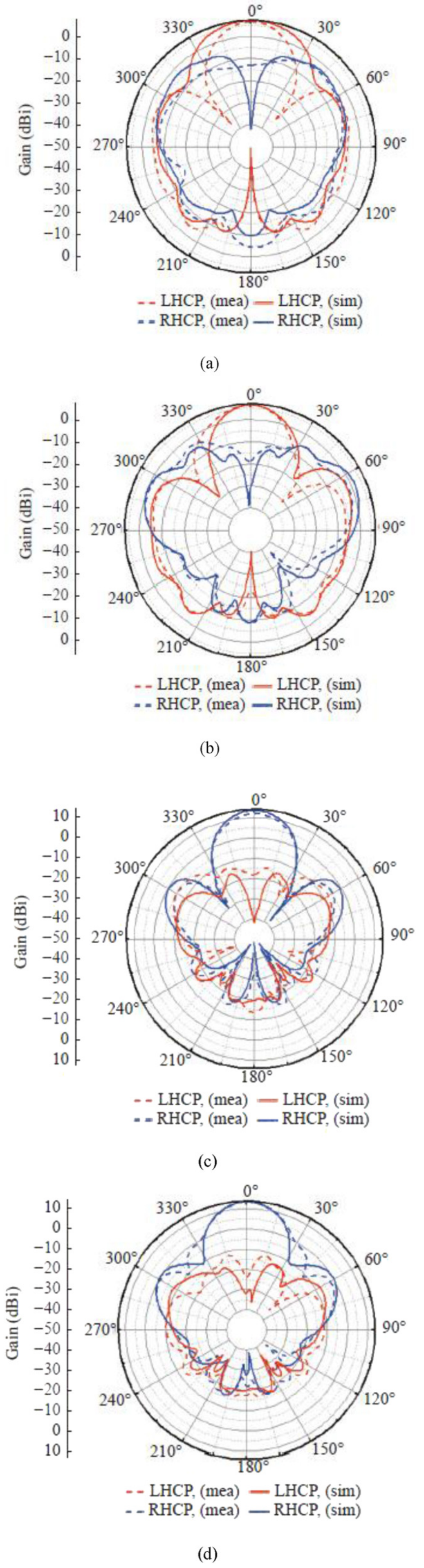

FIGURE 19
Radiation performance evaluation of the antenna array. **(a)** *xOz* plane at 17 GHz; **(b)** *yOz* plane at 17 GHz; **(c)** *xOz* plane at 28 GHz; **(d)** *yOz* plane at 28 GHz.

TABLE 3 Performance comparison of the proposed and existing designs.

Reference	Antenna type	Frequency band	Impedance bandwidth (%)	Axis ratio bandwidth (%)	Working bandwidth (%)	Polarization mode	Gain (dBi)
[7]	Magnetoelectric dipole; dual-frequency dual-circular polarization	Low frequency High frequency	12.4 4.6	5.0 9.7	5.0 4.6	LHCP RHCP	13.2 11.5
[14]	DRA; broadband dual circular polarization	Broadband	53.5	4.1 10.9	4.1 10.9	RHCP LHCP	4.8 4.8
[15]	DRA; dual-frequency dual-circular polarization	Low frequency High frequency	30.3 4.4	12.6 11.9	12.6 4.4	LHCP RHCP	5.0 2.4
[17]	DRA; dual-frequency dual-circular polarization	Low frequency High frequency	6.4 12.8	5.2 4.1	5.2 4.1	RHCP LHCP	6.6 8.2
[75]	DRA; dual-frequency dual circular polarization	Low frequency High frequency	7.3 11.4	9.8 10.1	11.3 4.3	LHCP RHCP	3.8 5.4
[77]	DRA; broadband dual circular polarization	Low frequency High frequency	6.8 12.3	8.8 3.5	10.5 4.1	LHCP RHCP	4.1 5.6
Proposed (unit)	DRA; dual-frequency dual-circular polarization	Low frequency High frequency	31.3 16.8	22.9 5.2	18.8 5.2	LHCP RHCP	4.3 6.8
Proposed (array)	DRA; dual-frequency dual-circular polarization	Low frequency High frequency	38.5 15.3	25.5 6.5	25.5 6.5	LHCP RHCP	7.7 14.0

Data availability statement

The original contributions presented in the study are included in the article/supplementary material, further inquiries can be directed to the corresponding authors.

Author contributions

MS: Conceptualization, Methodology, Project administration, Software, Investigation, Resources, Formal Analysis, Visualization, Writing – original draft, Writing – review and editing, Data curation. NS: Methodology, Writing – review and editing, Investigation, Supervision, Writing – original draft, Data curation, Resources, Conceptualization, Project administration, Visualization. MP: Project administration, Formal Analysis, Supervision, Writing – original draft, Methodology, Visualization, Conceptualization, Investigation, Writing – review and editing, Validation, Software. JK: Software, Writing – original draft, Supervision, Formal Analysis, Writing – review and editing, Conceptualization, Methodology, Data curation, Project administration, Resources, Validation. HT-H: Formal Analysis, Visualization, Project administration, Validation, Data curation, Resources, Funding acquisition, Supervision, Methodology, Software, Writing – review and editing, Conceptualization, Investigation, Writing – original draft. TH-T: Visualization, Methodology, Conceptualization, Validation, Writing – original draft, Formal Analysis, Supervision, Writing – review and editing, Data curation, Software. IQ: Writing – original draft, Data curation, Investigation, Methodology, Conceptualization, Writing – review and editing, Software, Resources, Validation, Formal Analysis. HM: Resources, Writing – review and editing, Conceptualization, Writing – original draft, Project administration, Validation, Formal Analysis, Supervision, Software, Data curation, Visualization. DA: Conceptualization, Writing – review and editing, Methodology, Supervision, Formal Analysis, Investigation, Visualization, Resources, Writing – original draft, Project administration.

Funding

The author(s) declared that financial support was received for this work and/or its publication. Princess Nourah bint Abdulrahman University Researchers Supporting Project number (PNURSP2026R140), Princess Nourah bint Abdulrahman University, Riyadh, Saudi Arabia. The authors would like to express their deepest gratitude to Universiti Kuala Lumpur (UniKL) for the invaluable support toward the completion and publication of this paper. This article has been produced with the financial support of the European Union under the REFRESH – Research Excellence For REgion Sustainability and High-tech Industries project number CZ.10.03.01/00/22_ 003/0000048 via the Operational Programme Just Transition.

Conflict of interest

The author(s) declared that this work was conducted in the absence of any commercial or financial relationships that could be construed as a potential conflict of interest.

Generative AI statement

The author(s) declared that generative AI was not used in the creation of this manuscript.

Any alternative text (alt text) provided alongside figures in this article has been generated by Frontiers with the support of artificial intelligence and reasonable efforts have been made to ensure accuracy, including review by the authors wherever possible. If you identify any issues, please contact us.

Publisher's note

References

1. Liu H, Yang Z, Gao Y, Dong L, Guo Y, et al. High-frequency gain enhancement of a broadband metasurface antenna with parasitic patches using characteristics mode analysis. *Front Phys* (2025) 13:1–10. doi:10.3389/fphy.2025.1638385

2. Lin X, Wu Z, Wang S, Zhong ZP, Lai YX, Zhang Y. A simple structure dual-band dual-circularly polarized antenna with controlled frequency ratio. *IEEE Access* (2022) 10:126687–94. doi:10.1109/access.2022.3225450

3. Fujimoto T, Guan C. A printed hybrid-mode antenna for dual-band circular polarization with flexible frequency ratio. *Electronics* (2025) 14(13):1–14. doi:10.3390/electronics14132504

4. Sridhar P, Poonkuzhali R. A dual-band circular polarized CPW fed low-profile antenna for WLAN and X-band applications. *Results Eng* (2025) 27(1):1–14. doi:10.1016/j.rineng.2025.106466

5. Xu Y, Zhu L, Liu N, Li M. A dual-band dual-circularly-polarized slow antenna with stable in-band gain and reduced frequency ratio under triple resonance. *IEEE Trans Antennas Propagation* (2022) 70(11):10199–206. doi:10.1109/tap.2022.3191133

6. Zheng Q, Ma J, Wu Z, Mohammadi P. Dual-broadband high-isolation circularly polarized low-RCS shared aperture antenna array based on mushroom-type metasurface. *Opt Commun* (2025) 574:1–13. doi:10.1016/j.optcom.2024.131127

7. Shirzad H, Ghobadi C, Nourinia J. Circularly polarized dual-band dipole antenna utilizing a transmissive type linear to circular polarization converter. *AEU-international J Electronics Commun* (2023) 166:1–14. doi:10.1016/j.aeue.2023.154649

8. Liu Y, Yue Z, Jia Y, Xu Y, Xue Q. Dual-band dual-circularly polarized antenna array with printed ridge gap waveguide," *IEEE Trans Antennas Propagation* (2021) 69, 8, 5118–23. doi:10.1109/tap.2020.3048504

9. An S, Kim B. Wideband multi-layered dielectric resonator antenna with small form factor for 5G millimeter-wave Mobile applications. *Electronics* (2025) 14(19):1–14. doi:10.3390/electronics14193756

10. Salucci M, Oliveri G, Hannan M, Azaro R, Massa A. Wide-band wide-beam circularly-polarized slow-coupled antenna for wide-angle beam scanning arrays. *Sensors* (2023) 23(3):1–16. doi:10.3390/s23031123

11. Omam Z, Shad S, Khalichi B, Mehrpouyan H, Khalily M, Kishk A. Wideband beam-steering flat dielectric lens antenna for 5G communications. *IEEE Access* (2025) 13:76914–22. doi:10.1109/access.2025.3565474

12. Gharbi M, Garcia R, Gil I. Wireless communication platform based on an embroidered antenna sensor for real-time breathing detection. *Sensors* (2022) 22(22):1–13. doi:10.3390/s22228667

13. Wang Y, Yang X. A dual-band dual-sense circularly polarized antenna based on chiral structure. *Microwave Opt Technology Lett* (2023) 65(6):1747–54. doi:10.1002/mop.33613

14. Amir A, Munkyo S. Size-reduction of a dual-band circularly polarized dielectric resonator antenna. *IEEE Access* (2021) 9:126457–65. doi:10.1109/ACCESS.2021.3107055

15. Zhao P, Ren J, Liu Y, Zhou Z, Yin Y. Wideband dual-feed dual-sense circularly polarized dielectric resonator antenna. *IEEE Trans Antennas Propagation* (2020) 68(12):7785–93. doi:10.1109/tap.2020.2999754

16. Mao C, Jiang Z, Werner D, Gao SS, Hong W. Compact self-duplexing dual-band dual-sense circularly polarized array antenna with closely spaced operating frequencies. *IEEE Trans Antennas Propagation* (2019) 67(7):4617–25. doi:10.1109/tap.2019.2911274

17. Xu H, Chen Z, Liu H, Chang L, Huang T, Ye S, et al. Single-fed dual-circularly polarized stackled dielectric resonator antenna for K/Ka-band satellite communications. *IEEE Trans Vehicular Technology* (2022) 71(4):4449–53. doi:10.1109/tvt.2022.3144414

18. Raj H, Sakshi K, Upender P. Dual-band circularly polarized dielectric resonator antenna with machine learning-assisted optimization and measured validation. *Electromagnetics* (2025) 1(2):1–11. doi:10.1016/j.rinp.2025.108531

19. Yin W, Si J, Li C, Khamas S. Dual-band aperture-shared antenna with pattern and polarization diversities for ISM applications. *J Electromagn Waves Appl* (2025) 39(15):1858–71. doi:10.1080/09205071.2025.2530627

20. Yan Q, Wei L, Xie Z. Dual band dual circularly polarized patch antenna for Ku-band applications. *AEU-international J Electronics Commun* (2024) 175(1):1–14. doi:10.1016/j.aeue.2023.155107

21. Xu J, Lan B, Zhang J, Guo C, Ding J. A novel dual-band dual-polarized shared-aperture antenna with high isolation. *Int J Microwave Wireless Tech* (2020) 12(7):652–9. doi:10.1017/s1759078719001454

22. Yu L, Wan J, Yang X, Shao S, Bai L, Xi Y, et al. Compact dual-band, dual-circularly polarized shared-aperture antenna based on the structure reuse of a DR. *IEEE Antennas Wireless Propagation Lett* (2025) 24(4):788–92. doi:10.1109/lawp.2024.3504519

23. Xiao Y, He L, Wei X. Dual-band dual-circularly polarized shared-aperture phased array for S-/C-band satellite communications. *Electronics* (2025) 14(2):1–15. doi:10.3390/electronics14020387

24. Gaya A, Jamaluddin M, Alali B, Althuwaib A. A novel wide dual band circularly polarized dielectric resonator antenna for milli meter wave 5G applications. *Alexandria Eng J* (2022) 61(12):10791–803. doi:10.1016/j.aej.2022.04.025

25. Yadav S, Gupta A, Kumar V, Gard D, Gburi A. Prediction of axial ratio using machine learning (ML) for a dual-band circularly polarized dielectric resonator antenna (DRA). *Chin J Phys* (2025) 96:1364–84. doi:10.1016/j.cjph.2025.07.008

26. Lou T, Yang X, Tan G, Gao S. Shared aperture dual-band dual circularly polarized multibeam antenna for satellite-assisted internet of vehicles. *IEEE Internet Things J* (2023) 11(7):12000–11. doi:10.1109/jiot.2023.3332092

27. Tong X, Jiang Z, Li Y, Wu F, Wu J, Sauleau R, et al. An integrated dual-band dual-circularly polarized shared-aperture transmit-array antenna for K-/Ka-band applications enabled by polarization twisting elements. *IEEE Trans Antennas Propagation* (2023) 71(6):4955–66. doi:10.1109/tap.2023.3263214

28. Ran J, Jin C, Wang W, Chen J, Wu Y. Dual-band dual-linearly/circularly polarized shared-aperture antenna for satellite communication systems. *AEU-international J Electronics Commun* (2022) 148:1–14. doi:10.1016/j.aeue.2022.154156

29. He M, Tu Z, Nie N. Dual-band dual-circularly polarized aperture-shared antenna based on SIW for millimeter-wave/Sub-6 GHz communication applications. *Microwave Opt Technology Lett* (2025) 67(3):1–15. doi:10.1002/mop.70163

30. Wu T, Zhang Z. Millimeter-wave broadband dual-circularly polarized array antenna loaded with metasurface. *Scientific Rep* (2025) 15:1–15. doi:10.1038/s41598-025-22109-9

31. Dai M, Sun G, Yu H, Niyato D. Maximize the long-term average revenue of network slice provider via admission control among heterogeneous slices. *IEEE/ACM Trans Networking* (2024) 32(1):745–60. doi:10.1109/TNET.2023.3297883

32. Sun G, Xu Z, Yu H, Chang V. Dynamic network function provisioning to enable network in box for industrial applications. *IEEE Trans Ind Inform* (2021) 17(10):7155–64. doi:10.1109/TII.2020.3042872

33. Zhang H, Xu Y, Luo R, Mao Y. Fast GNSS acquisition algorithm based on SFFT with high noise immunity. *China Commun* (2023) 20(5):70–83. doi:10.23919/JCC.2023.00.006

34. Yao Y, Shu F, Cheng X, Liu H, Miao P, Wu L. Automotive radar optimization design in a spectrally crowded V2I communication environment. *IEEE Trans Intell Transportation Syst* (2023) 24(8):8253–63. doi:10.1109/TITS.2023.3264507

35. Zhou G, Huang J, Li H, Li Y, Jia G, Song N, et al. Multispectral camouflage and radiative cooling using dynamically tunable metasurface. *Opt Express* (2024) 32(7):12926–40. doi:10.1364/OE.517889

36. Li L, Cherouat A, Snoussi H, Wang T. Grasping with occlusion-aware ally method in complex scenes. *IEEE Trans Automation Sci Eng* (2025) 22:5944–54. doi:10.1109/TASE.2024.3434610

37. Hu J, Jiang H, Xiao Z, Chen S, Dustdar S, Liu J. HeadTrack: real-time human–computer interaction *via* wireless earphones. *IEEE J Selected Areas Commun* (2024) 42(4):990–1002. doi:10.1109/JSAC.2023.3345381

38. Hu J, Jiang H, Liu D, Xiao Z, Zhang Q, Liu J, et al. Combining IMU with acoustics for head motion tracking leveraging wireless earphone. *IEEE Trans Mobile Comput* (2024) 23(6):6835–47. doi:10.1109/TMC.2023.3325826

39. Hu J, Jiang H, Liu D, Xiao Z, Dustdar S, Liu J. A wireless self-service system for library using commodity RFID devices. *IEEE Internet Things J* (2024) 11(3):4998–5010. doi:10.1109/JIOT.2023.3301462

40. Li D, Li P, Zhao J, Liang J, Liu J, Liu G, et al. Ground-to-UAV sub-terahertz channel measurement and modeling. *Opt Express* (2024) 32(18):32482–94. doi:10.1364/OE.534369

41. Li J, Sun R, Wang Y, Ochieng WY. A robust time synchronization algorithm for GNSS/IMU integrated navigation in urban environments. *Meas Sci Technology* (2025) 36(3):036302. doi:10.1088/1361-6501/ada9a2

42. Deng J, Gao N, Chen X. Ultrawide attenuation bands in gradient metabeams with Acoustic black hole pillars. *Thin-Walled Structures* (2023) 184:110459. doi:10.1016/j.tws.2022.110459

43. Gao N, Huang Q, Pan G. Ultra-broadband sound absorption characteristics in underwater ultra-thin metamaterial with three layer bubbles. *Eng Rep* (2024) 6(11):e12939. doi:10.1002/eng2.12939

44. Gao N, Guo X, Deng J, Cheng B, Hou H. Elastic wave modulation of double-leaf ABH beam embedded mass oscillator. *Appl Acoust* (2021) 173:107694. doi:10.1016/j.apacoust.2020.107694

45. Zeng Z, Goetz SM. A general modeling and analysis of impacts of unbalanced inductance on PWM schemes for two-parallel interleaved power converters. *IEEE Trans Power Electronics* (2024) 39(10):12235–48. doi:10.1109/TPEL.2024.3388024

46. Fan S, Han C, He K, Bai L, Chen L, Shi H, et al. Acoustic moiré flat bands in twisted Heterobilayer metasurface. *Adv Mater* (2025) 37(29):2418839. doi:10.1002/adma.202418839

47. Xu H, Wei H, Chen H, Chen Z, Zhou X, Xu H, et al. Effect of periodic phase modulation on the matched filtering with insufficient phase-shift capability. *IEEE Trans Aerospace Electron Syst* (2025) 61(3):5755–70. doi:10.1109/TAES.2024.3520959

48. Xu G, Xu S, Fan X, Cao Y, Mao Y, Xie Y, et al. RAT ring: event driven publish/subscribe communication protocol for IIoT by report and traceable ring signature. *IEEE Trans Ind Inform* (2025) 21(9):6670–8. doi:10.1109/TII.2025.3567265

49. Yin X, Li X, Qian L, Zhu Z. Numerical Analysis and Optimization of Chip-Level Drop Impact Reliability for Chiplet Based on Si Interposer. *IEEE Trans Components, Packaging Manufacturing Technology* (2025) 15(6):1203–12. doi:10.1109/TCPMT.2025.3566026

50. Wang F, Zhang S, Hong E, Quek TQS. Constellation as a service: tailored connectivity management in direct-satellite-to-device networks. *IEEE Commun Mag* (2025) 63:1–7. doi:10.1109/MCOM.001.2500138

51. Chang H, Feng S, Qiu X, Meng H, Guo G, He X, et al. Implementation of the toroidal absorption cell with multi-layer patterns by a single ring surface. *Opt Lett* (2020) 45(21):5897–900. doi:10.1364/OL.404198

52. Xu Y, Liu Y, Lei M, Gao M, Fang Z, Jiang C. Joint pseudo-range and doppler positioning method with LEO satellites‘ signals of opportunity. *Satellite Navigation* (2025) 6(1):10. doi:10.1186/s43020-025-00163-y

53. Wei J, Lin H. Reliability-oriented routing of internal current stress in the two-stage SST submodule. *IEEE Trans Power Electronics* (2025) 41:1–11. doi:10.1109/TPEL.2025.3595961

54. Wu T, Li M, Qu Y, Wang H, Wei Z, Cao J. Joint UAV deployment and edge association for energy-efficient federated learning. *IEEE Trans Cogn Commun Networking* (2025) 1. doi:10.1109/TCCN.2025.3543365

55. Lei Y, Dong S, Liang R, Xiang S, Huang Q, Ma J, et al. Parallel resonant magnetic field generator for biomedical applications. *IEEE Trans Biomed Circuits Syst* (2025) 19(3):496–510. doi:10.1109/TBCAS.2024.3450881

56. Zhang K, Wang H, Chen M, Chen X, Liu L, Geng Q, et al. Leveraging machine learning to proactively identify phishing campaigns before they strike. *J Big Data* (2025) 12(1):124. doi:10.1186/s40537-025-01174-x

57. Xu G, Wang L, Chen S, Zhu L, Guizani M, Shi L. MPAEE: a multipath adaptive energy-efficient routing scheme for low Earth orbit-based industrial internet of things. *IEEE Internet Things J* (2025) 12(17):34793–805. doi:10.1109/JIOT.2025.3581314

58. Zou X, Wang Y, Zong B, Xu X, Han L, Zhu H, et al. Miniaturized low-profile ultrawideband antipodal vivaldi antenna array loaded with edge techniques. *IEEE Trans Antennas Propagation* (2025) 1:1. doi:10.1109/TAP.2025.3606193

59. Meng Z, Shen F, Gazor S. WLB-CANUN: widely linear beamforming in coprime array with non-uniform noise. *IEEE Trans Vehicular Technology* (2025) 74(4):5833–42. doi:10.1109/TVT.2024.3504278

60. Yin R, Peng J, Cai Y, Wu C, Champagne B, Al-Dhahir N. Radar-assisted predictive beamforming for UAV-aided networks: a deep-learning solution. *IEEE Trans Vehicular Technology* (2025) 74:1–15. doi:10.1109/TVT.2025.3572037

61. Liu S, Shen Y, Yuan J, Wu C, Yin R. Storage-Aware joint user scheduling and bandwidth allocation for federated edge learning. *IEEE Trans Cogn Commun Networking* (2025) 11(1):581–93. doi:10.1109/TCCN.2024.3451711

62. Wu Z, Ismail M, Zhang J, Zhang J. Tidal-Like concept drift in RIS-covered buildings: when programmable wireless environments meet human behaviors. *IEEE Wireless Commun* (2025) 32:1–8. doi:10.1109/MWC.2025.3600792

63. Zhang K, Zheng B, Xue J, Zhou Y. Explainable and trust-aware AI-Driven network slicing framework for 6G IoT using deep learning. *IEEE Internet Things J* (2025) 1:1. doi:10.1109/JIOT.2025.3619970

64. Sun R, Sheng Q, Cheng Q, Shang X, Ochieng WY. 3-D grid-based resilient pseudorange error prediction for adaptive GNSS/IMU integrated navigation in urban areas. *IEEE Internet Things J* (2025) 12(12):19264–79. doi:10.1109/JIOT.2025.3533077

65. Xu G, Fan X, Xu S, Cao Y, Zhang K, Kang J, et al. Towards authenticated encrypted search with constant trapdoor for Mobile cloud systems. *IEEE Trans Mobile Comput* (2025) 1–15. doi:10.1109/TMC.2025.3627241

66. Feng R, Yu Y, Wu L, Wang J, Tan Q, Burokur SN. Full-space programmable metasurface for bessel beam tailoring. *Opt Lett* (2025) 50(16):5161–4. doi:10.1364/OL.570659

67. Feng D, Bai B, Ma J, Yuan W, Li S, Jiang J. Multi-domain index modulation for MIMO-OTFS and A coarse-to-fine network for detection. *IEEE Trans Wireless Commun* (2025) 1:2389–403. doi:10.1109/TWC.2025.3596372

68. Liu L, Wang F, Yin X, Xu M, Yang Y, Yu N, et al. Low-loss flexible filter based on compact double interdigital coupling SIR with TPV technology for bendable wireless communications. *IEEE Microwave Wireless Technology Lett* (2025) 1–4. doi:10.1109/LMWT.2025.3637823

69. Yang N, Gao H, Ju S, Zhang Z, Zhao Y, Guo X, et al. Achieving broadband electromagnetic absorption in laminated composites through progressive Bayesian optimization. *Composites B: Eng* (2025) 307:112882. doi:10.1016/j.compositesb.2025.112882

70. Zhu N, Zhang Y, Zhao Z, Meng F. Design of a compact wideband SPDT switch with high isolation for Sub-6 GHz applications. *IEEE Trans Circuits Syst Express Briefs* (2025) 1:43–7. doi:10.1109/TCSII.2025.3638907

71. Zhang Y, Zhu N, Meng F, Wang K, Ma K, Yeo KS. Design and analysis of a compact CMOS SOI power amplifier with 29.2-dBm P SAT and 44.4% PAE for FR3 5G-Advanced/6G beamforming systems. *IEEE J Solid-State Circuits* (2025) 1–14. doi:10.1109/JSSC.2025.3639947

72. Zhou Z, Abawajy J, Chowdhury M, Hu Z, Li K, Cheng H, et al. Minimizing SLA violation and power consumption in cloud data centers using adaptive energy-aware algorithms. *Future Generation Computer Syst* (2018) 86:836–50. doi:10.1016/j.future.2017.07.048

73. Zhou Z, Shojafar M, Alazab M, Abawajy J, Li F. AFED-EF: an energy-efficient VM allocation algorithm for IoT applications in a cloud data center. *IEEE Trans Green Commun Networking* (2021) 5(2):658–69. doi:10.1109/TGCN.2021.3067309

74. Yu W, Ma C, Ma Y, Ma G, Wang H, Zhou Y, et al. Boosting electromagnetic wave absorbing capacity of Al2O3 coating through *in situ* generating nano

TiO1.81 from Ti2AlC MAX phases. *Adv Funct Mater* (2025) 35(39):2504393. doi:10.1002/adfm.202504393

75. Yang D, Sheng H, Wang S, Wang S, Xiong Z, Ke W. Boosting light field spatial super-resolution *via* masked light field modeling. *IEEE Trans Comput Imaging* (2024) 10:1317–30. doi:10.1109/TCI.2024.3451998

76. Ding X, Xu Y, Li G, Yang K, Yuan J, An J. Design and performance evaluation for BILCM-ID system with improved stopping criterion. *IEEE Trans Vehicular Technology* (2025) 74(4):6779–84. doi:10.1109/TVT.2024.3519540

77. Huang H, Zhang W, Xu Y, Zhang H, Zou J. A method for PWM frequency harmonic suppression using zero-vector switching SVPWM strategy in three-level inverter drive systems. *IEEE J Emerging Selected Top Power Electronics* (2025) 13(2):1482–91. doi:10.1109/JESTPE.2024.3485962

78. Zhou D, Sheng M, Bao C, Wang Y, Li J, Han Z. Mission-driven resource scheduling in satellite-terrestrial networks: from perspective of collaboration and reconfiguration. *IEEE Trans Commun* (2025) 73(8):6705–19. doi:10.1109/TCOMM.2025.3529250